Journal of Geophysical Research: Space Physics

RESEARCH ARTICLE
10.1029/2018JA025603

Key Points:
- High-frequency THEMIS data of a BICI head crossing are compared with PIC simulations
- Electromagnetic ion cyclotron instability waves rippled the head
- Differential drift between the electrons and ions drives the instability

Correspondence to:
E. V. Panov,
evgeny.panov@oeaw.ac.at

Citation:
Panov, E. V., & Pritchett, P. L. (2018). Ion cyclotron waves rippling Ballooning/InterChange Instability heads. *Journal of Geophysical Research: Space Physics*, *123*, 8261–8274. https://doi.org/10.1029/2018JA025603

Received 23 APR 2018
Accepted 21 SEP 2018
Accepted article online 28 SEP 2018
Published online 27 OCT 2018

Ion Cyclotron Waves Rippling Ballooning/InterChange Instability Heads

E. V. Panov[1] **and P. L. Pritchett**[2]

[1]Space Research Institute, Austrian Academy of Sciences, Graz, Austria, [2]Department of Physics and Astronomy, University of California, Los Angeles, CA, USA

Abstract A dawnward drifting Ballooning/InterChange Instability (BICI) head is identified and studied using high-resolution Time History of Events and Macroscale Interactions during Substorms observations at $X_{GSM} \approx -11R_E$ on 15 February 2008 between 10:18 UT and 10:30 UT and compared with particle-in-cell simulation run results for a charged current sheet. A prediction of the earlier particle-in-cell simulation for a neutral sheet, that duskward drifting BICI heads are subject to a current-driven ion cyclotron instability, is found to be true also for dawnward drifting BICI heads in the charged sheet simulations. This specific prediction and the Time History of Events and Macroscale Interactions during Substorms data indicate the presence of electromagnetic ion cyclotron wave activity that ripples the background BICI head shape. The waves propagated azimuthally with $\delta E_y/\delta B_z \approx 4.5V_A$. The waves are found in a region of the strongest differential drift between the electrons and ions, suggesting that the drift generated the waves.

1. Introduction

Growing direct and indirect evidence of magnetic field minima presence in the transition region between the dipole and tail fields (Sergeev et al., 2018, and references therein) raises the possible importance of the instabilities that may be driven by such magnetotail configurations. Among them are instabilities of the interchange type whose wavelength is finite parallel to the magnetic field, that is, the ballooning instabilities (Rosenbluth & Longmire, 1957). Such instabilities have been suggested to occur in the transition region based on geosynchronous GOES (Roux et al., 1991) and near-Earth's plasma sheet Cluster observations (Baumjohann et al., 2007).

Modern particle-in-cell (PIC) treatment of a current sheet with a tailward gradient of B_z, part of a magnetic field minimum configuration, has revealed growth of a kinetic Ballooning/InterChange Instability (BICI; Pritchett & Coroniti, 2010; Sitnov et al., 2014). BICI generates azimuthally confined earthward intruding depleted plasma tubes (heads) with the characteristic field-aligned electron flows. The head development may lead to onset of reconnection (Pritchett & Coroniti, 2011, 2013). Time History of Events and Macroscale Interactions during Substorms (THEMIS) observations showed that sausage-type magnetic oscillations that propagate duskward across the near-Earth plasma sheet at $X_{GSM} \approx -11R_E$ and could be followed by a substorm onset indeed exhibit field-aligned electron flows and other BICI signatures (Panov, Nakamura et al.,2012; Panov, Sergeev et al., 2012).

Pritchett et al. (2014) suggested that BICI may be one possible source of dipolarization fronts (Nakamura et al., 2002) and the corresponding auroral streamers (Nakamura et al., 2001), because the latter appeared to break into the substructures. Pritchett and Coroniti (2010) showed that the dominant wave components of the BICI mode are in the electrostatic potential $\delta\Phi$ and $\delta B_{||}$ and thus are the same as for the lower-hybrid drift instability in a straight geometry. For an off-equatorial plasma sheet configuration with a dominant B_x geocentric solar magnetospheric (GSM) field, these would correspond to δE_y, δE_z, and δB_x wave fields. Thus, BICI appears to be a low-frequency generalization of lower-hybrid drift instability to a curved magnetic field geometry. In its linear stage, the BICI heads were observed to drift duskward (in the direction of the equilibrium ion drift) with a speed of about $0.12V_{Ti}$, where V_{Ti} is the ion thermal speed. This was for the case of a charge-neutral current sheet. At late stages, however, the BICI heads moved dawnward due to the development of a $E_x \times B_z$ drift resulting from an earthward directed E_x field at the head.

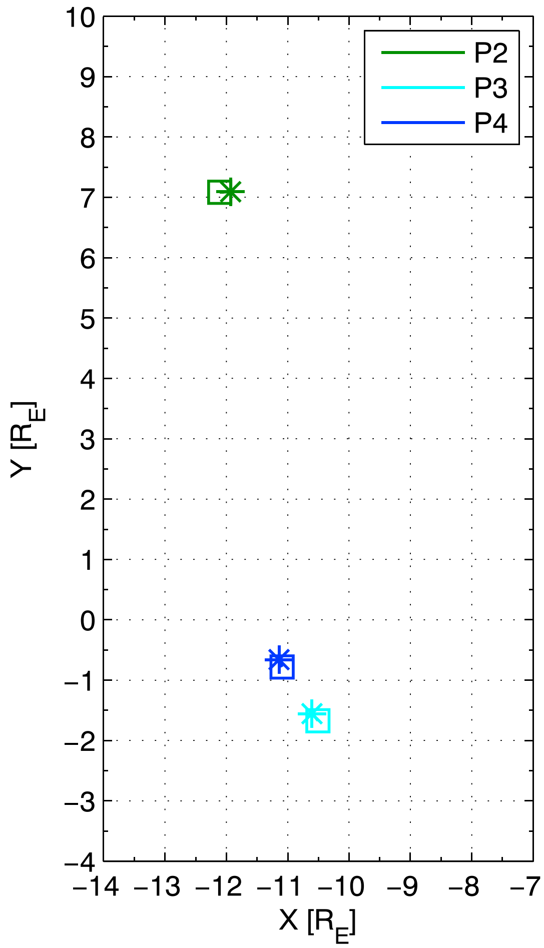

Figure 1. Orbit segments for Time History of Events and Macroscale Interactions during Substorms probes P2 (green), P3 (cyan), and P4 (blue) on 15 February 2008 between 10:18 UT (stars) and 10:30 UT (squares) in XY geocentric solar magnetospheric plane.

Pritchett et al. (2014) observed that, still for a charge-neutral sheet, the BICI heads were accompanied by strong off-equator waves with frequency of the order of the ion gyrofrequency, which could be the reason for the breaking of the streamer into the substructures. These waves appeared to match the properties of the electromagnetic ion cyclotron instability (Perraut et al., 2000), which are left hand polarized and strongly compressional. In the simulation, these waves propagated westward with a speed of about $0.5V_{Ti}$, although at late times there was some indication that this speed decreased (Figure 10a in Pritchett et al., 2014). Spectral signatures of the waves with frequency of the order of the ion gyrofrequency were recently found at earthward propagating dipolarization fronts (Huang et al., 2012, 2015; Zhang et al., 2017; Zhou et al., 2014).

Motivated by the hypothesis of Pritchett et al. (2014), in the present investigation we carry out a detailed comparison of azimuthally drifting structures observed by THEMIS (Angelopoulos, 2008) at $X_{GSM} \approx -11R_E$ with the characteristics of the BICI heads predicted by PIC simulations. Magnetotail observations were provided by the probes' fluxgate magnetometers (Auster et al., 2008), electrostatic analyzers' (McFadden et al., 2008) particle detectors, and electric field instruments (Bonnell et al., 2008). We use three-point observations of a BICI head crossing by azimuthally separated THEMIS probes P2–P4 on 15 February 2008 between 10:18 UT and 10:30 UT to reveal that the head propagated dawnward. We perform an analysis of the Nishimura et al. (2016) PIC run to confirm that the ion cyclotron instability operates also in the dawnward drifting BICI regime. We further use rare high-resolution (burst mode) THEMIS probe P4 electromagnetic and particle data during the BICI head crossing to demonstrate that the head was subject to a current-driven ion cyclotron instability, which rippled the background BICI head shape, and that the instability grew in a region of strong differential electron-ion drift.

The outline of the paper is as follows. Section 2 demonstrates the dawnward propagation and structure of a BICI head as seen by THEMIS probes P2–P4 and compares these with the predictions of the PIC simulations in a charged current sheet. Burst mode THEMIS probe P4 observations and PIC simulation predictions of the off-equator wave modes are discussed in section 3. The differences in electron and ion distribution functions and flows inside and between the BICI heads are considered in section 4. Sections 5 and 6 provide discussion and conclusions. Appendix A describes the PIC simulation model and initial equilibrium configuration.

2. BICI Head Examples From THEMIS and PIC

2.1. Cross-Tail Drift of a BICI Head by THEMIS

Figure 1 shows orbit segments for THEMIS probes P2 (green), P3 (cyan), and P4 (blue) on 15 February 2008 between 10:18 UT (stars) and 10:30 UT (squares) in XY GSM plane. The three probes were separated mainly in the Y_{GSM} direction, with the most duskward P2 located near $Y_{GSM} = 7.1R_E$ and the most dawnward P3 around $Y_{GSM} = -1.7R_E$. P4 was located about 1 R_E duskward and about 0.5 R_E tailward from P3. Hence, such spacecraft configuration is ideal for studying of magnetotail structures that propagate in the azimuthal direction, for example, BICI heads.

Figure 2 shows THEMIS spin-averaged B_z magnetic and E_y electric field GSM components on 15 February 2008 between 10:18:00 UT and 10:30:00 UT from probes P2 (first and second panels), P4 (third and fourth panels), and P3 (fifth and sixth panels). The three probes consequently observed a dawnward drifting structure (seen as B_z and E_y enhancements) whose leading edge was met first by P2 at ∼10:19:52 UT, then by P4 at ∼10:23:20 UT, and finally by P3 at ∼10:23:48 UT (indicated by the green, blue, and cyan vertical lines); that is, the time delay of the structure's leading edge observations was about 208 s between P2 and P4 and about 28 s between P4 and P3. Hence, the dawnward propagation velocity of the structure's leading edge is about 49,652 km/208 s≈239 km/s, if estimated using P2/P4 and about 5,748 km/28 s ≈205 km/s using P3/P4. Note

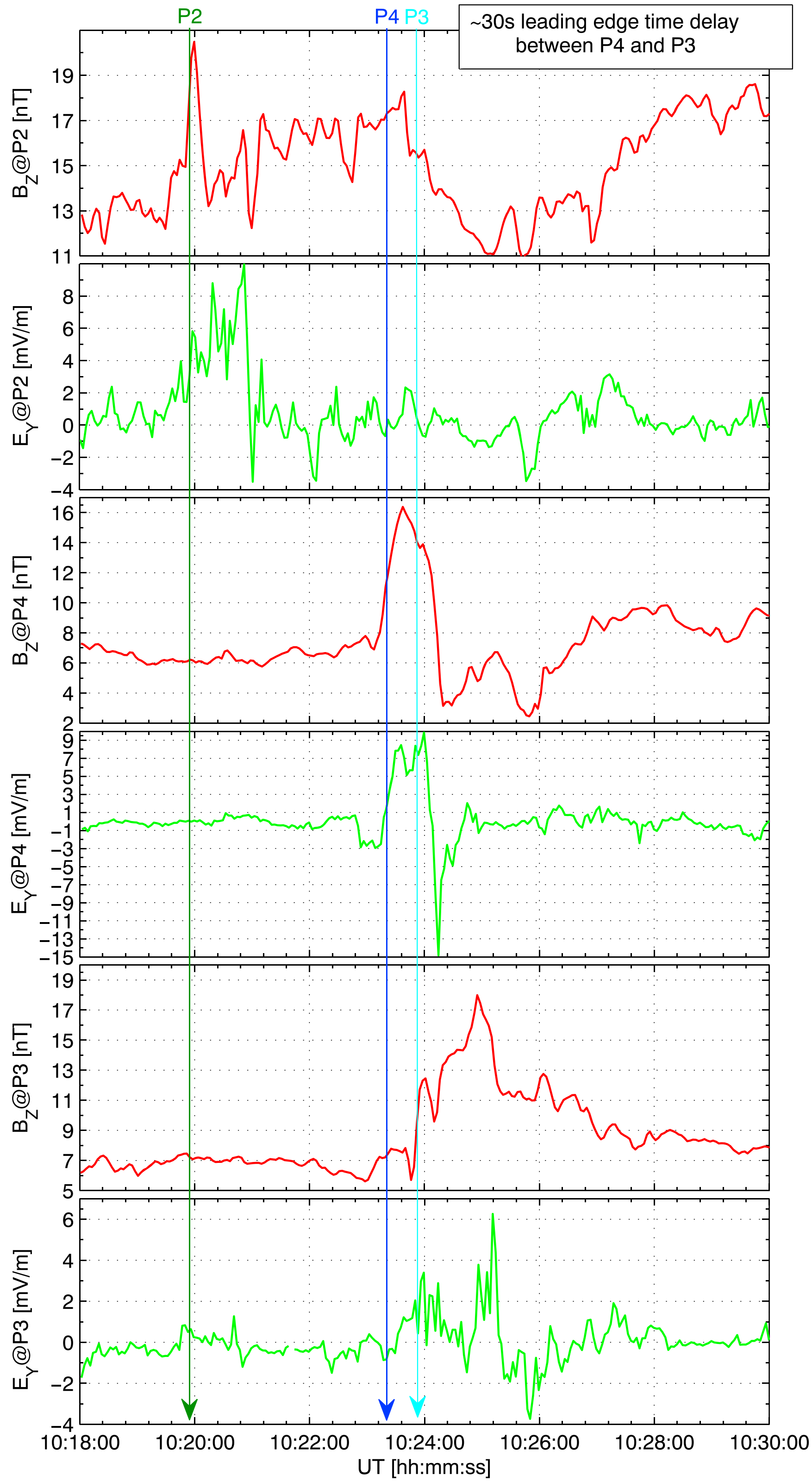

Figure 2. Time History of Events and Macroscale Interactions during Substorms spin-averaged B_z magnetic and E_y electric field geocentric solar magnetospheric components on 15 February 2008 between 10:18:00 UT and 10:30:00 UT from probes P2 (first and second panels), P4 (third and fourth panels), and P3 (fifth and sixth panels). The head's leading edge as detected by the three probes is indicated by the green, blue, and cyan vertical lines.

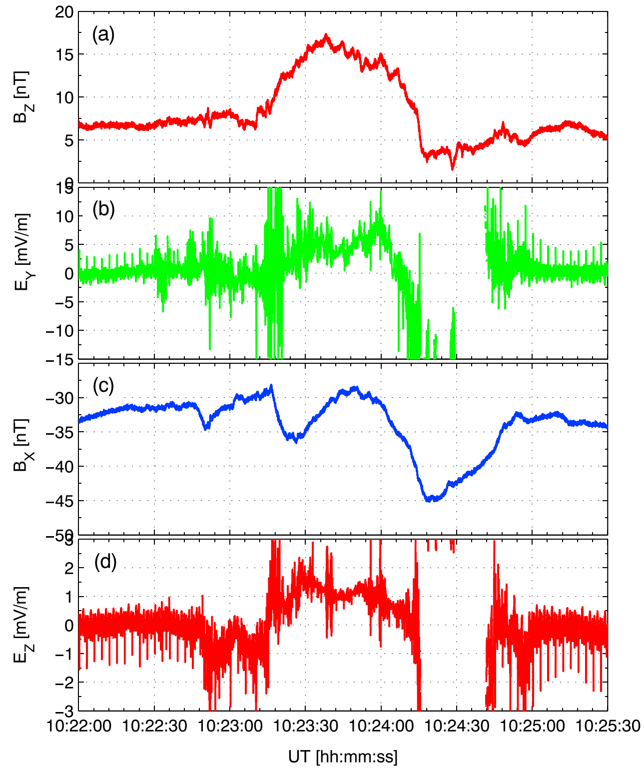

Figure 3. Time History of Events and Macroscale Interactions during Substorms probe P4 observations on 15 February 2008 between 10:22:00 UT and 10:25:30 UT: from top to bottom geocentric solar magnetospheric components of (a) B_z, (b) E_y, (c) B_x, and (d) E_z. The electric field components were calculated assuming $(E \cdot B) = 0$.

that the ambiguity in identification of the leading edge crossing times may contribute to an error in the velocity estimates of up to about 50 km/s (or about 20%). The corresponding structure azimuthal scale (as seen in B_z) varied between about 0.8 R_E (at P2) and 1.8 R_E (2.5 R_E) at P4 (P3). Note that the azimuthal scale of the structure in P2 observations is ambiguous because the width of the B_z enhancement is significantly smaller than the width of the corresponding E_y enhancement, with the E_y enhancement width being close to P3/P4 observations. The structure in Figure 2 is one of many similar structures that were observed on 15 February 2008 between 9:00 UT and 11:00 UT by P2–P5. All of these structures had a similar spatial scale and propagated dawnward at a similar velocity, and they exhibited general properties of the duskward propagating BICI heads (Panov & Pritchett, 2018). The structure's azimuthal propagation velocity (of about 0.35 times the ion thermal velocity) and its scale, as well as a number of other signatures, discussed in the next section, allow us to identify this structure as a magnetotail BICI head.

2.2. BICI Head Structure

On 15 February 2008 between 10:20:30 UT and 10:30:20 THEMIS probe P4 collected fields and particle data at 128-Hz cadence. Together with the BICI head motion analysis from Figure 2, this constitutes a unique data set that permits carrying out investigations of the fine structure of the BICI head observed by P4 around 10:23:20 UT. Figure 3 shows THEMIS observations of (from top to bottom) B_z, E_y, B_x, and E_z GSM components on 15 February 2008 between 10:22:00 UT and 10:25:30 UT. The electric field components were calculated assuming $(E \cdot B) = 0$; they are contaminated with spurious quasiperiodic spikes (from $E_{X,DSL}$), four times per spin, due to sphere shadowing by the spacecraft body that do not affect our results.

The BICI head was observed as a pronounced B_z enhancement between 10:23:10 UT and 10:24:15 UT (Figure 3a). Between 10:23:30 UT and 10:24:10 UT one can also recognize smaller-scale oscillations in B_z with amplitudes of about 1–2 nT. The B_z enhancement is associated with the positive average $E_y \approx 5$ mV/m (Figure 3b). At the leading and the trailing edges of the BICI head (i.e., at the sharp gradients in B_y around 10:23:17 UT and 10:24:15 UT) E_y also exhibited high-frequency ($f > f_{LH}$) oscillations, which will be studied elsewhere. Around the trailing edge of the BICI head (between 10:23:30 UT and 10:24:30 UT) B_x exhibited a bipolar

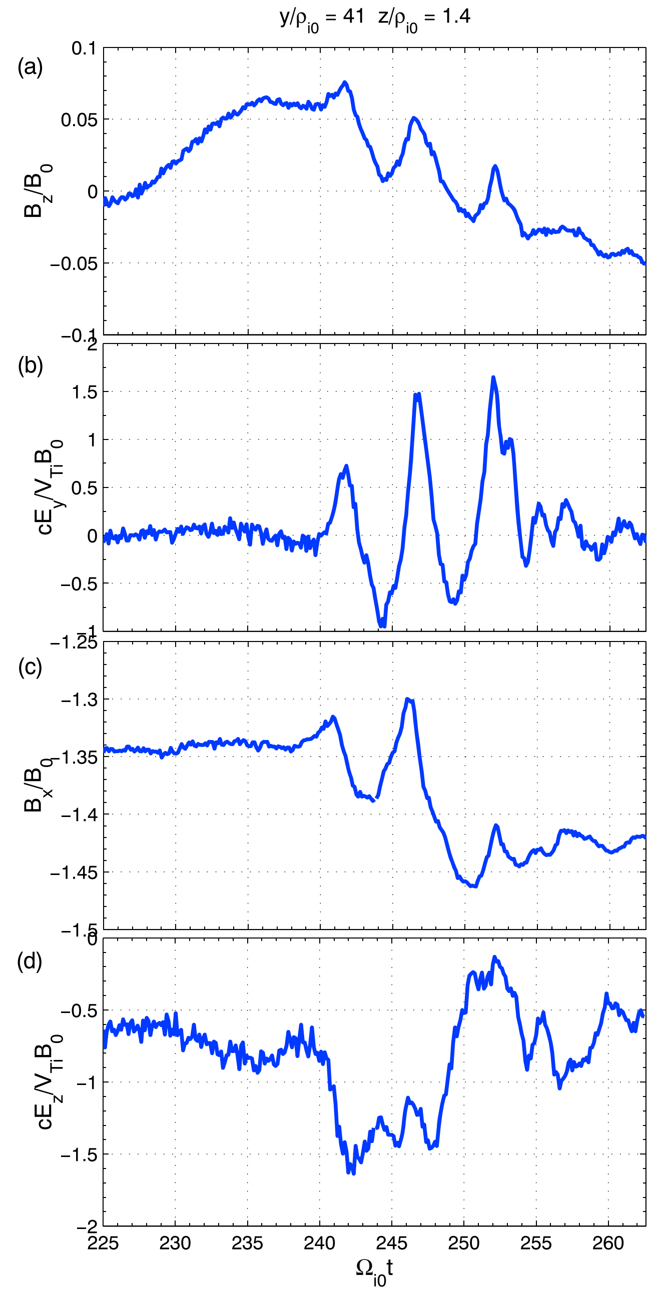

Figure 4. Time variation at a single point $x/\rho_{i0} = 6, y/\rho_{i0} = 41, z/\rho_{i0} = 1.4$ of various field components for the charged sheet simulation during one Ballooning/InterChange Instability head passing: (a) B_z/B_0, (b) $cE_y/V_{T_i}B_0$, (c) B_x/B_0, and (d) $cE_z/V_{Ti}B_0$.

variation (Figure 3c). Enhanced E_z field directed toward the center of the plasma sheet (Figure 3d; P4 was in the Southern Hemisphere) was observed during the B_z enhancement.

One can make a direct comparison of the above THEMIS probe P4 observations with the 3-D PIC simulations for the charged sheet by plotting the electric and magnetic field components against simulation time for a specific point. Figure 4 shows time variation at a single point $x/\rho_{i0} = 6, y/\rho_{i0} = 41, z/\rho_{i0} = 1.4$ of the same field components as in Figure 3: (a) B_z/B_0, (b) $cE_y/V_{T_i}B_0$, (c) B_x/B_0, and (d) $cE_z/V_{Ti}B_0$. While the magnitude of B_z is drastically different between the THEMIS example and the simulation, the actual difference for the mesoscale jump in B_z relative to the lobe field in each case is only a factor of 2 (0.2 vs. 0.1). A bipolar-like variation around the trailing edge of the BICI head ($240 \leq \Omega_{i0}t \leq 255$) in B_x (Figure 4c) and the E_z field directed toward the center of the current sheet (the chosen point at $z/\rho_{i0} = 1.4$ is in the Northern Hemisphere) peaking around the center of the BICI head ($\Omega_{i0}t \approx 245$, Figure 4d) are both seen in the PIC simulations, in accord with P4 observations in Figures 3c and 3d.

3. Electromagnetic Ion Cyclotron Instability

3.1. Ion Cyclotron Waves Rippling BICI Head

As in the P4 observations (Figure 3a), the simulations reveal electromagnetic waves that are clearly seen in B_z and E_y (Figures 4a and 4b). The actual amplitude of the wave oscillation itself (≈1 nT) on the few second timescale is actually very similar in both P4 observations and PIC simulations. Based on the local field strength $B_T/B_0 = 1.35$, the frequency of the oscillations in Figures 4a and 4b is 0.9 of the local ion cyclotron frequency. For the THEMIS observations in Figure 3 this would correspond to a period of the order of 1.5–2 s. The oscillations within the elevated B_z hump between 10:23:30 UT and 10:24:00 UT in Figure 3a are of a similar timescale (1.5–4 s).

Figure 5 shows wavelet spectra of the B_z GSM magnetic field (top panel) and of the E_y DSL electric field (bottom panel) components from THEMIS probe P4 on 15 February 2008 between 10:22:00 UT and 10:25:30 UT. The proton cyclotron frequency estimated using the total magnetic field B_T is indicated by magenta curves and using B_z is indicated by the dark blue curves. The power spectral densities appeared to be enhanced during the BICI head crossing in the frequency range between 0.1 and 0.6 Hz, that is, close to the local proton cyclotron frequency.

Figure 6 shows band-pass-filtered (in the frequency range between 0.1 and 0.6 Hz) GSM components of the electric field δE (top), of the magnetic field δB (middle), and of the Poynting flux (bottom) calculated from δE and δB from THEMIS probe P4 between 10:22:00 UT and 10:25:30 UT. Indeed, the observed electromagnetic waves with frequencies near the local proton cyclotron frequency reveal larger amplitudes around the BICI head, and decay before ($t \leq$10:22:30 UT) and after it ($t \geq$10:25:00 UT).

Propagation axis of circularly polarized electromagnetic waves can be estimated with the help of the minimum variance analysis (Sonnerup & Scheible, 1998). The minimum variance analysis applied to the filtered magnetic field data between 10:23:20 UT and 10:23:50 UT (central part of the BICI head) reveals that the minimum variance direction is directed mostly azimuthally at (−0.04; −0.99; 0.16) GSM and hence indicates an azimuthal propagation of the electromagnetic waves near the local proton cyclotron frequency. The minimum variance direction of the waves observed before 10:23:20 UT (leading edge of the BICI head) and after 10:23:50 UT (trailing edge of the BICI head) appeared to be at about 45° to the Y_{GSM} axis and suggests an oblique propagation of the waves at the BICI head edges.

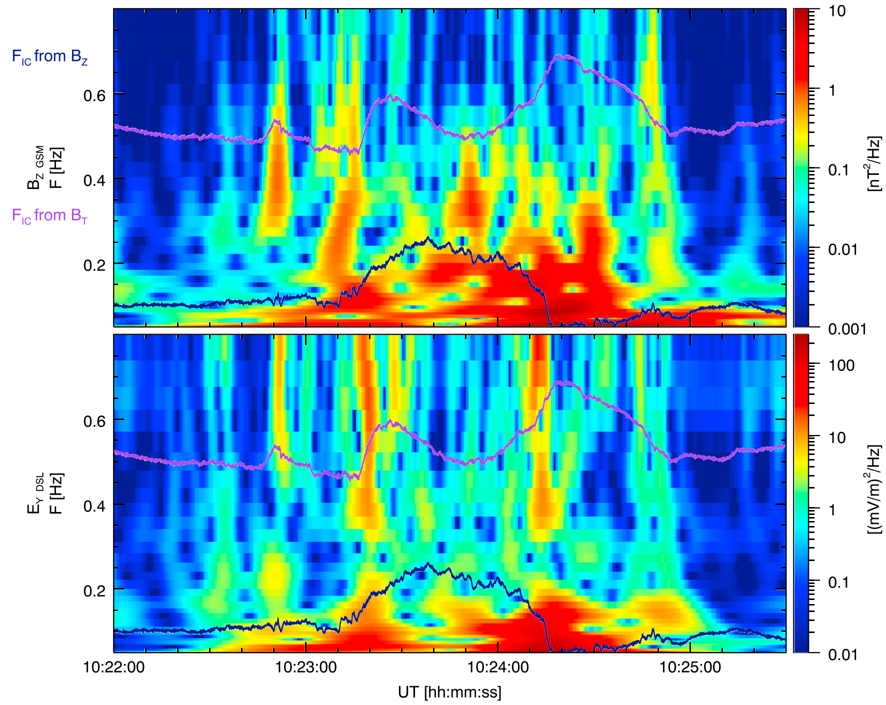

Figure 5. Wavelet spectra of the B_Z geocentric solar magnetospheric magnetic field (top panel) and of the E_y Despun SunSensor L-vectorZ (DSL) electric field (bottom panel) components from Time History of Events and Macroscale Interactions during Substorms probe P4 on 15 February 2008 between 10:22:00 UT and 10:25:30 UT. The proton cyclotron frequency was estimated using the total magnetic field B_T (magenta curves) and B_Z (dark blue curves).

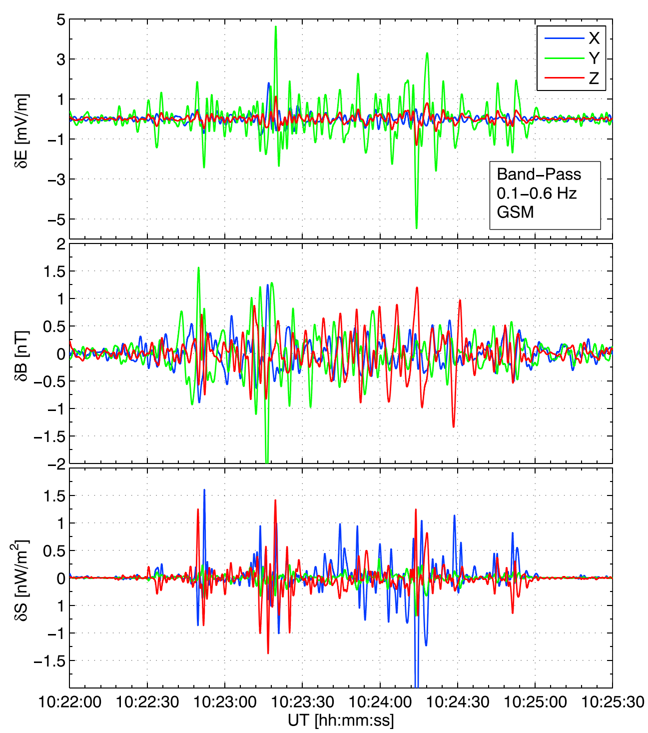

Figure 6. Band-pass (between 0.1 and 0.6 Hz)-filtered GSM components of the electric field δE (top), of the magnetic field δB (middle), and of the Poynting flux (bottom) calculated from δE and δB from Time History of Events and Macroscale Interactions during Substorms probe P4 between 10:22:00 UT and 10:25:30 UT. GSM = geocentric solar magnetospheric.

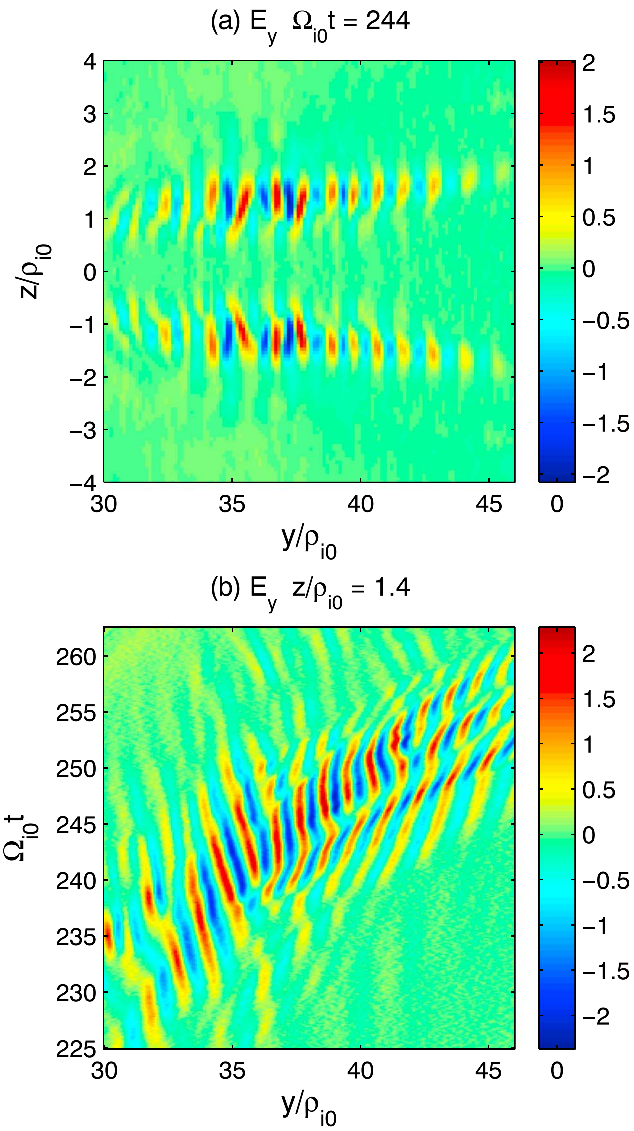

Figure 7. Results from 3-D particle-in-cell simulation for the electromagnetic ion cyclotron waves in one Ballooning/InterChange Instability head for charged sheet: y, z cut of E_y (a) at $x/\rho_{i0} = 6$ at time $\Omega_{i0}t = 244$. Stack plot showing the time development of the wave fields at the fixed point $x/\rho_{i0} = 6, z/\rho_{i0} = 1.4$ (b).

Taking average amplitudes of δE_y and δB_z in Figure 6 between 10:23:20 UT and 10:23:50 UT of about 0.5 mV/m and 0.5 nT, one obtains the $\delta E_y/\delta B_z$ ratio of the order of 1,000 km/s. Assuming the total magnetic field inside the BICI head of 40 nT and the ion density of 0.2 cm^{-3}, the local Alfvén speed is about $V_A \approx$220 km/s. Hence, $\delta E_y/\delta B_z \approx 4.5V_A$. This value is consistent with the $\delta E/\delta B$ estimate from PIC simulations (Pritchett et al., 2014) and exceeds by about 4 times the dawnward propagation velocity of the BICI head. The Poynting vector is in the XY GSM plane, with the Poynting flux sometimes peaking above 1 nW/m^2 (bottom panel in Figure 6).

3.2. Ion Cyclotron Wave Propagation

Figure 7 illustrates the bidirectional propagation of the off-axis wave modes in the charged sheet simulation. Figure 7a shows a y, z cut at $x/\rho_{i0} = 6$ at time $\Omega_{i0}t = 244$ for E_y. The strongest wave fields are in the range $34 < y/\rho_{i0} < 38$ and $|z/\rho_{i0}| \sim 1.4$. Figure 7b is a stack plot showing the time development of the wave fields at the fixed point $x/\rho_{i0} = 6, z/\rho_{i0} = 1.4$. For time $\Omega_{i0}t < 245$ and $y/\rho_{i0} < 36$, the structures are propagating duskward. This is the natural propagation direction for the ion cyclotron waves. However, for time $\Omega_{i0}t > 245$ and $y/\rho_{i0} > 36$, the propagation direction shifts to dawnward. A similar shift at late times from duskward to dawnward propagation was seen in the original BICI simulation for a neutral sheet (Pritchett & Coroniti, 2010).

This shift can be understood from Figure 8a that shows the $(E \times B)_y$ drift component at $\Omega_{i0}t = 244$. For the strongest E_y fields (roughly $34 < y/\rho_{i0} < 38$) the $E \times B$ velocity is essentially 0, and the waves propagate duskward. However, for $y/\rho_{i0} > 38$, there is a strong (comparable to V_{Ti}) $E \times B$ flow at the z location of the waves. This arises due to a local E_x field directed earthward from the BICI head. This is due to electron Hall currents that flow around the BICI head and is large enough to overcome the duskward motion of the ion cyclotron waves.

In order to compare the predicted by the PIC simulations $E \times B$ development with THEMIS observations, we employ P4 observations in Figures 8b and 8c. For the same time interval as in Figure 6, the blue curve in Figure 8c shows spin-averaged component $(E \times B)_Y/B^2$ of the $E \times B$ drift velocity. In accord with Figure 8a, the major contribution to $(E \times B)_Y/B^2$ was indeed provided by the $(-E_xB_z)/B^2$ term (red curve in Figure 8c). $(E \times B)_Y/B^2$ in Figure 8b between 10:23:25 UT and 10:24:05 UT is between about −400 and −1,300 km/s. These values are comparable to the above estimates of $\delta E_y/\delta B_z$, and hence, the earthward E_x (Figure 8b between about 10:23:30 UT and 10:24:00 UT) may indeed overcome the natural duskward motion of the ion cyclotron waves.

4. Electron and Ion BICI Flows

In the PIC simulations the free energy source for the electromagnetic ion cyclotron waves was found to be the differential drift between the electrons and the ions (Pritchett et al., 2014). Figure 9 shows y, z cuts of the parallel component of the electron velocity (a) and of the x component of the ion velocity (b) for one BICI head for the charged sheet. The results are plotted in a y, z plane cut at $x/\rho_{i0} = 6$ at time $\Omega_{i0}t = 244$. The electron parallel flows are quite large; they reach $\sim V_{Ti}$ in the region of the off-axis oscillations, and they exhibit bipolar variations between positive and negative flows on the scale of the ion oscillations ($1-2\rho_{i0}$). The off-axis ion velocity U_{ix} is about 20% of the electron parallel velocity, but it is unidirectional (despite some modulation), unlike the electron flow.

Figure 10 shows THEMIS probe P4 observations of the electron (a) and ion (b) velocity GSM components on 15 February 2008 between 10:22:00 UT and 10:25:30 UT. In accordance with the PIC simulation results from Figure 9, the ion velocity peaks at about 100 km/s which is about 20% of the peak electron velocity (500 km/s)

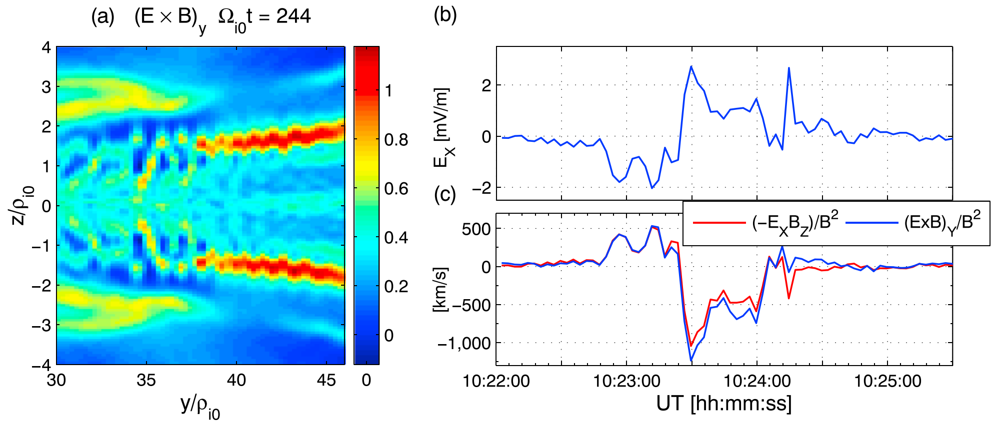

Figure 8. The y, z cut of $(E \times B)_y/(B^2 V_{Ti})$ at $x/\rho_{i0} = 6$ at time $\Omega_{i0}t = 244$ (a). Spin-averaged E_x and components of the $E \times B$ drift velocity as observed by Time History of Events and Macroscale Interactions during Substorms probe P4 on 15 February 2008 between 10:22:00 UT and 10:25:30 UT (b and c). See color coding for details.

at 10:23:45 UT. The electron data are 15-s sliding-window averaged to suppress thermal noise. Since electrostatic analyzers' particle detectors' time resolution is only 3 s, THEMIS particle data are unable to resolve the fine structure of the electron flow predicted by the PIC simulations. In the present case V_{Ti} was about 650 km/s (Figure 10e). Taking $V_{ix}/V_{Ti} \approx 0.2$, the predicted V_{ix} of 130 km/s is fairly close to the observed values. Note that inside the BICI head (between about 10:23:30 UT and 10:24:30 UT) the density is depleted, in accord with the idea that the BICI head has a reduced entropy (Figure 10c).

Figure 11 shows ion (top row) and electron (bottom row) distribution functions during single BICI head observation by THEMIS probe P4 on 15 February 2008 between 10:23:17 UT and 10:23:23 UT (left column), and between 10:23:38 UT and 10:23:50 UT (right column). The functions are shown in the *BV* coordinates in which the abscissa is parallel to the magnetic field and the bulk velocity defines the ordinate. Whereas the left column in Figure 11 corresponds to the leading edge of the BICI head, the right column in the figure reveals the particle distribution functions in the middle of the head.

The ion beams are unidirectional (top row in Figure 11) and directed oppositely inside and outside of the head, in accord with the PIC simulation results in the top panels of Figure 11 in Pritchett et al. (2014). The bottom row in Figure 11 reveals bidirectional parallel electron beams. This looks different from the PIC simulation results that are shown in the bottom panels of Figure 11 in Pritchett et al. (2014) where the corresponding electron distribution functions showed only a single direction for the electron beam. However, the simulations and the THEMIS data are not inconsistent with each other. The THEMIS distributions were accumulated over 6 or 12 s. Since the BICI heads are drifting dawnward at 200–240 km/s, the data sample a portion of the head of length 1,200–2,880 km, which is about 2–5 times the ion cyclotron mode wavelength. The simulation plots in Figure 11 of Pritchett et al. (2014) were taken at two values of *y* that differed by only half of the mode wavelength. That is why they showed only a single direction for the electron beam. The direction of the electron drift reverses with the phase of the wave.

5. Discussion

Taking advantage of unique high-resolution in situ observations during one dawnward propagating BICI head crossing permitted an investigation of the details of the head's structure and a direct comparison with the PIC simulation for a charged current sheet. Along with consistency between the observations and the PIC simulation for the macroscale BICI structures, the principal new finding was the observation of the development of the electromagnetic ion cyclotron waves across the head.

The center of the time interval with the pronounced wave activity shown in Figures 5 and 6 appears to coincide with the strongest differential drift between the electrons and ions (around 10:23:45 UT in Figure 10). The whole time interval with the wave activity coincides with the time interval of enhanced $(E \times B)_Y/B^2$ values in Figure 8b. A detailed comparison of the electromagnetic ion cyclotron waves revealed by the PIC simulations with linear theory of the current-driven Alfvén instability waves (Perraut et al., 2000) was presented in Pritchett et al. (2014). According to Perraut et al. (2000), even a modest parallel drift V_d between the electrons

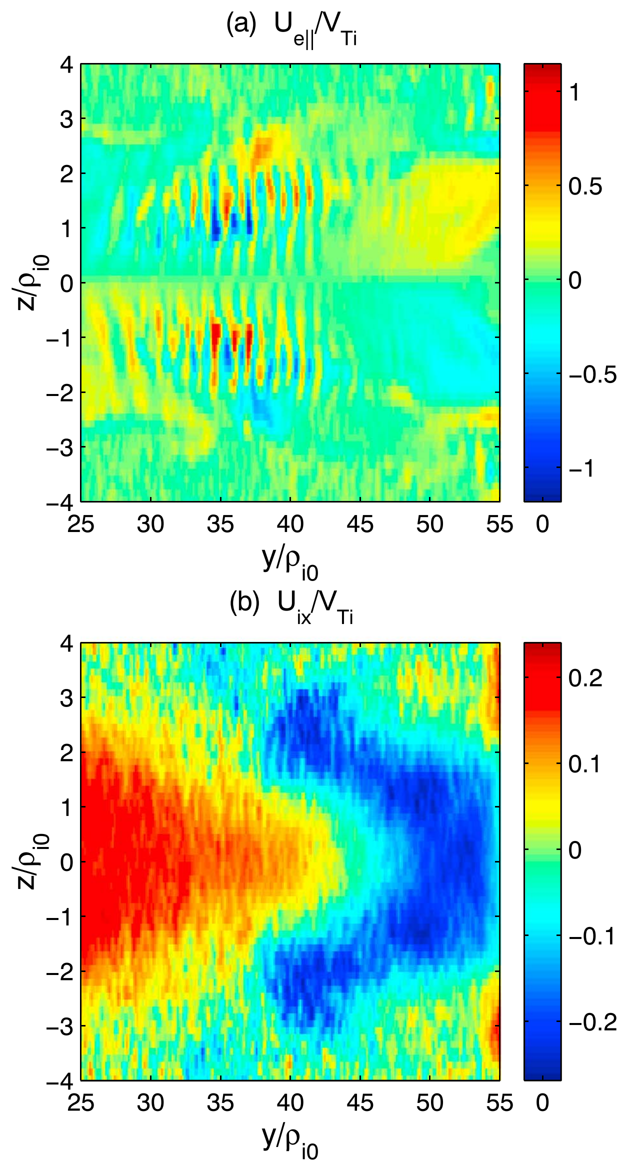

Figure 9. The y, z cuts of the parallel component of the electron velocity (a) and of the x component of the ion velocity (b) for one Ballooning/InterChange Instability head in a charged sheet at $x/\rho_{i0} = 6$ at time $\Omega_{i0}t = 244$.

and ions can destabilize current-driven Alfvén instability waves (already with V_d of about 0.03 times the electron thermal velocity V_{Te}; in the present study V_d was comparable to this value, cf. Figure 10d). The coincidental appearance of the large differential electron-ion drift along the magnetic field and of the waves whose properties match those predicted by both theory (Perraut et al., 2000) and the present PIC simulations indicates that probably the parallel differential electron-ion drift has generated the waves.

In the current sheet with large plasma-to-magnetic-pressure ratio, BICI heads may lead to a localized reconnection (Pritchett & Coroniti, 2011, 2013). Such detached BICI heads would exhibit the properties that are attributed to the earthward propagating reconnection (dipolarization) fronts (Nakamura et al., 2002) including the sharp B_z variations that are embedded in a fast earthward plasma flow. Hence, if the electromagnatic ion cyclotron waves were developing at such a BICI head, they are also expected to be observed at an earthward dipolarization front that appeared as a detached BICI head. Indeed, there are documented observations of various wave activities near the ion cyclotron frequency at dipolarization fronts; some signatures of these waves were found to be consistent with the current-driven electromagnetic ion cyclotron instability (Huang et al., 2015; Zhang et al., 2017).

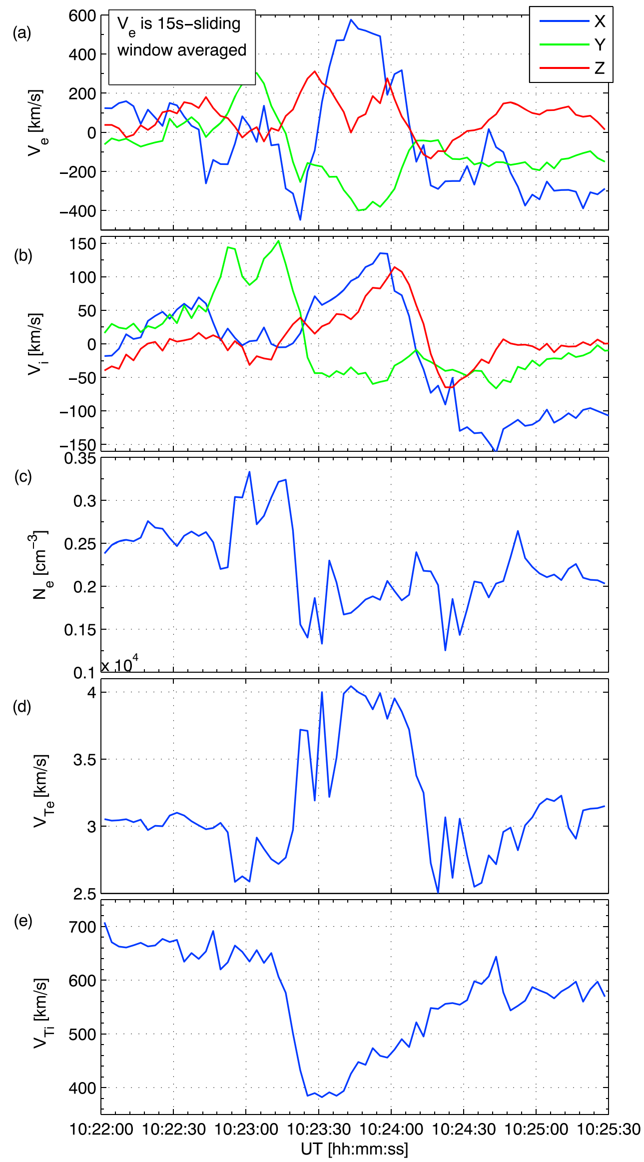

Figure 10. Time History of Events and Macroscale Interactions during Substorms probe P4 observations on 15 February 2008 between 10:22:00 UT and 10:25:30 UT: electron (a) and ion (b) velocity geocentric solar magnetospheric components, electron density (c), and electron (d) and ion (e) thermal velocity. Electron velocity data are 15-s sliding-window averaged to suppress noise.

Different possibilities of the magnetic minimum formation, such as simultaneous adiabatic lobe compression and sunward convection removing closed magnetic flux in the near-Earth tail (Hsieh & Otto, 2015), or creating a diamagnetic thin current sheet by imposition of a dawn to dusk electric field E_y (Pritchett & Coroniti, 1994, 1995), would lead to a neutral or charged thin current sheets. In the event under study the dawnward propagation of the BICI head suggests that the BICI developed in a charged thin current sheet.

Supported by an example of a structured auroral streamer captured by a THEMIS all sky imager, Pritchett et al. (2014) suggested that rippling and breakup of a reconnected BICI head by the electromagnetic ion cyclotron instability may be the reason for such structuring. Hence, it is important to carry out detailed analyses of conjugate high-resolution observations between BICI heads in the plasma sheet and their ionospheric footprints.

10.1029/2018JA025603

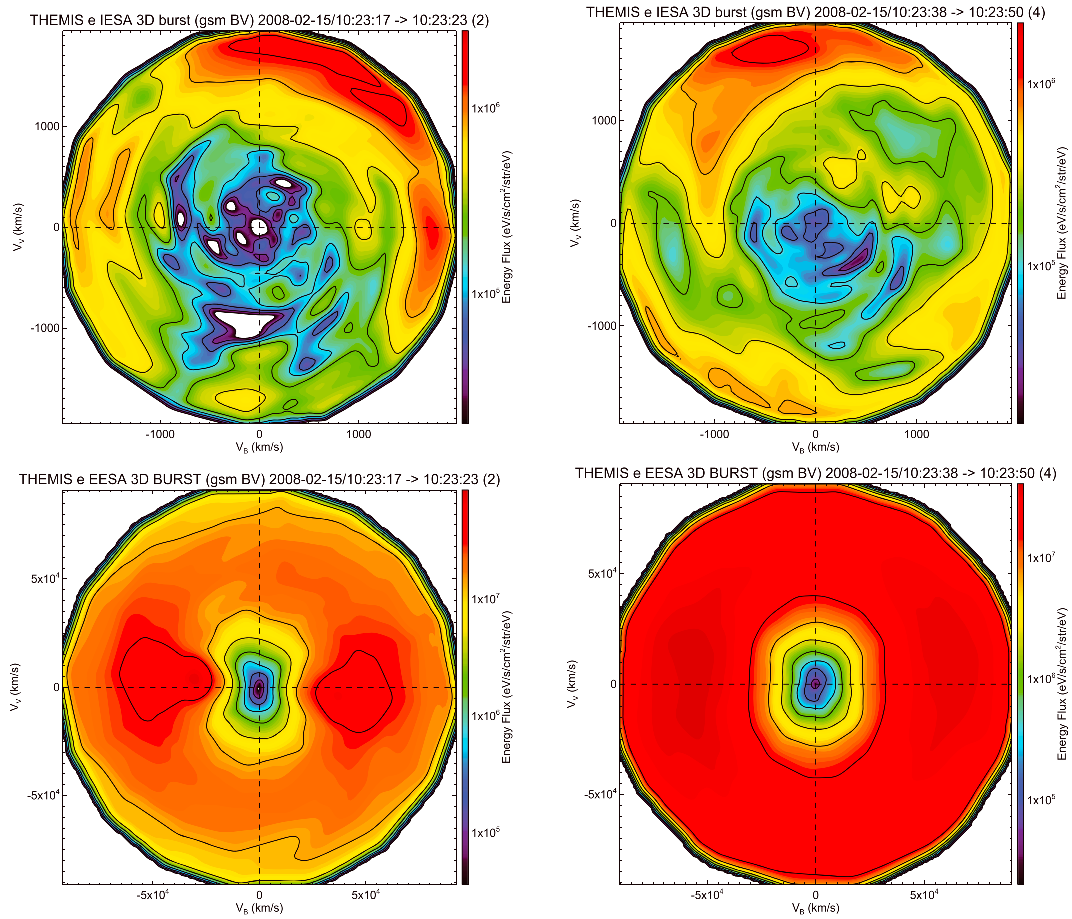

Figure 11. Ion (top row) and electron (bottom row) distribution functions during single Ballooning/InterChange Instability head observation by THEMIS probe P4 on 15 February 2008 between 10:23:17 UT and 10:23:23 UT (left column), and between 10:23:38 UT and 10:23:50 UT (right column). THEMIS = Time History of Events and Macroscale Interactions during Substorms.

6. Conclusions

Burst mode THEMIS observations of a dawnward drifting BICI head in the near-Earth plasma sheet at X_{GSM} around $-11\ R_E$ on 15 February 2008 between 10:18 UT and 10:30 UT reveal that the BICI head was subject to an electromagnetic ion cyclotron instability, which rippled the background BICI head shape. The large-scale structure of the BICI head and the properties of the ion cyclotron waves are consistent with the predictions made by the PIC simulations: the waves propagate azimuthally with $\delta E_y/\delta B_z \approx 4.5 V_A$. The waves are found in a region of the strongest differential drift between the electrons and ions, suggesting that the drift generated the waves.

Appendix A: PIC Simulation Setup

The present investigation employs a 3-D PIC simulation model that retains the full dynamics for both electrons and ions. The initial magnetic field configuration is similar to those considered previously in Pritchett and Coroniti (2010, 2013) and is described by the vector potential $A_{0y}(x,z)$ given by

$$A_{0y}(x,z) = B_0 L \ln\{\cosh[F(x)(z/L)]/F(x)\}, \tag{A1}$$

where $F(x)$ is a slowly varying but otherwise arbitrary function. For a nonconstant $F(x)$, there is a finite B_z field, which at the center of the current sheet has the form

$$B_{0z}(x,0) = -B_0 L F'(x)/F(x). \tag{A2}$$

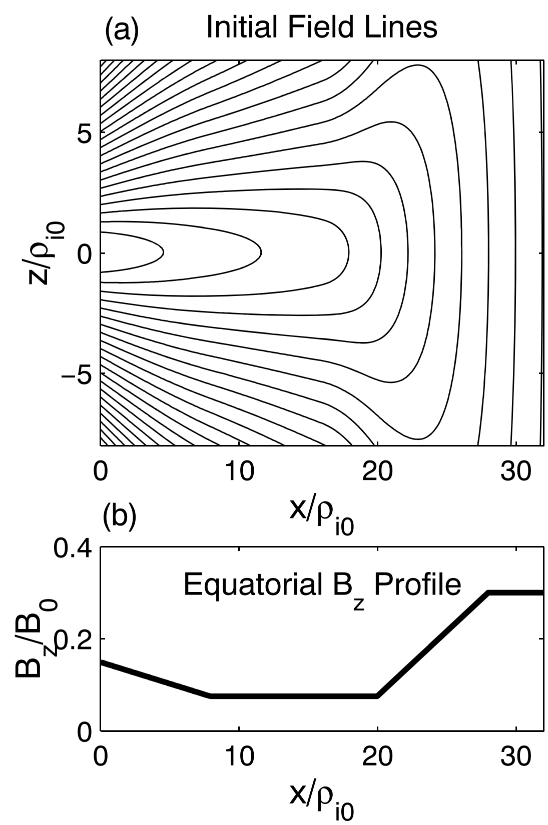

Figure A1. Specific initial particle-in-cell simulation configuration used in the present study: 2-D (x, z) magnetic field configuration (a), and initial equatorial magnetic field profile $B_{0z}(x, 0)$ (b).

The specific configuration used in the present study is illustrated in Figure A1. Figure A1a shows the 2-D (x, z) magnetic field configuration, and Figure A1b shows the initial equatorial magnetic field profile $B_{0z}(x, 0)$. The BICI modes will be excited in the region of the tailward gradient in B_z ($20 < x/\rho_{i0} < 28$), which corresponds to a region of decreasing entropy as x increases tailward (Pritchett & Coroniti, 2013; Schindler & Birn, 2004). Here ρ_{i0} is the ion gyroradius in the asymptotic lobe B_0 field.

Previous PIC simulations of BICI generation (Pritchett & Coroniti, 2010, 2013; Pritchett et al., 2014) have considered a charge neutral, generalized Harris configuration in which the ion and electron cross-tail drifts are given by $V_{di} = -2cT_i/eB_0L$ and $V_{de} = 2cT_e/eB_0L$, where e is the magnitude of the fundamental electric charge and L is the half-width of the current sheet. In the present study, we consider a charged current sheet in which the electrons carry all of the cross-tail current with a net drift of $V_{de}^{ch} = 2c(T_i + T_e)/eB_0L$. Since the ions now carry no current, an electric field $E_{0z}(x, z)$ must be present in order to balance the nonuniform ion pressure,

$$E_{0z}(x, z) = -(2T_i/eL)F(x)\tanh[F(x)(z/L)]. \tag{A3}$$

The (ion) density distribution is given by

$$n(x, z) = n_0F^2(x)sech^2[F(x)(z/L)] + n_b, \tag{A4}$$

where n_0 is the characteristic equatorial density at $x/\rho_{i0} = 16$ and $n_b = 0.08n_0$ is a constant background density. The density distribution for the current-carrying electrons is similar to that for the ions but with a larger characteristic density n_e given by $(n_e - n_0)/n_e = [T_i/(T_i + T_e)](V_{de}^{ch}/c)^2$.

The simulation has a grid $N_x \times N_y \times N_z = 512 \times 1{,}024 \times 256$ distributed over the ranges $0 \le x/\rho_i \le 32$, $0 \le y/\rho_{i0} \le 64$, and $-8 \le z/\rho_{i0} \le 8$, so that $\rho_{i0} = 16\Delta$, where Δ is the grid spacing. The ion to electron mass ratio is $m_i/m_e = 64$, all particle temperatures are equal to $m_iV_A^2/4$ (here $V_A = (B_0^2/4\pi n_0m_i)^{1/2}$ is a representative Alfvén speed), the electron plasma frequency/gyrofrequency ratio is $\sqrt{2}$, and the electron Debye length is Δ. The total number of particles in the simulation is 5.8 billion.

The simulation employs *closed* boundary conditions at the x boundaries (Pritchett & Coroniti, 1998). No magnetic flux is allowed to cross these boundaries, corresponding to the condition $\delta E_y = 0$, and particles that cross these boundaries are reinserted back into the system in the opposite half z plane with $v_x = -v_x$ and $v_z = -v_z$ (Pritchett et al., 1991). In addition, the perturbed field δE_z is assumed to vanish at these boundaries. At the z boundaries, conducting conditions are assumed, and particles striking such a boundary are reintroduced into the opposite half z plane with $v_x = -v_x$ and $v_z = v_z$. This symmetric condition on the particle reflection is valid in the absence of a guide magnetic field. Periodicity in the y direction is assumed for both the particles and fields. The coordinate system used in the simulations has x increasing tailward (away from the Earth), y directed dawnward, and z directed northward. In the simulation figures, the coordinates are expressed in units of ρ_{i0}.

Acknowledgments
We acknowledge NASA contract NAS5-02099 for use of data from the THEMIS Mission and, specifically, for the use of fluxgate magnetometer data supported through the German Ministry for Economy and Technology and the German Center for Aviation and Space (DLR) under contract 50 OC 0302. For the GBO/ASIs, we acknowledge S. Mende and E. Donovan, NASA contract NAS5-02099 and the CSA for logistical support in fielding and data retrieval from the GBO stations. The THEMIS data were obtained freely from Space Sciences Laboratory-University of California, Berkeley (ftp://themis.ssl.berkeley.edu/data/themis/). The work of P. L. P. was supported by NASA grant NNX14AF70G. The particle simulations were made possible by an allocation of advanced computing resources provided by the NASA High-End Computing (HEC) Program through the NASA Advanced Supercomputing (NAS) Division at Ames Research Center. The PIC simulation data can be obtained from pritchet@physics.ucla.edu. The work of E. V. P. was partly supported by the Austrian Science Fund (FWF): I 3506-N27. This paper was initiated from discussions within the framework of the international team *Explosive Processes in the Magnetotail: Reconnection Onset and Associated Plasma Instabilities* supported by the International Space Science Institute (ISSI), including two dedicated workshops held in Bern, Switzerland, in October 2016 and 2017.

References

Angelopoulos, V. (2008). The THEMIS mission. *Space Science Reviews*, *141*, 5–34. https://doi.org/10.1007/s11214-008-9336-1

Auster, H. U., Glassmeier, K. H., Magnes, W., Aydogar, O., Baumjohann, W., Constantinescu, D., et al. (2008). The THEMIS Fluxgate\jcode{} Magnetometer. *Space Science Reviews*, *141*, 235–264. https://doi.org/10.1007/s11214-008-9365-9

Baumjohann, W., Roux, A., Le Contel, O., Nakamura, R., Birn, J., Hoshino, M., et al. (2007). Dynamics of thin current sheets: Cluster observations. *Annales de Geophysique*, *25*, 1365–1389. https://doi.org/10.5194/angeo-25-1365-2007

Bonnell, J. W., Mozer, F. S., Delory, G. T., Hull, A. J., Ergun, R. E., Cully, C. M., et al. (2008). The Electric Field Instrument (EFI) for THEMIS. *Space Science Reviews*, *141*, 303–341. https://doi.org/10.1007/s11214-008-9469-2

Hsieh, M.-S., & Otto, A. (2015). Thin current sheet formation in response to the loading and the depletion of magnetic flux during the substorm growth phase. *Journal of Geophysical Research: Space Physics*, *120*, 4264–4278. https://doi.org/10.1002/2014JA020925

Huang, S. Y., Yuan, Z. G., Ni, B., Zhou, M., Fu, H. S., Fu, S., et al. (2015). Observations of large-amplitude electromagnetic waves and associated wave-particle interactions at the dipolarization front in the Earth's magnetotail: A case study. *Journal of Atmospheric and Solar-Terrestrial Physics*, *129*, 119–127. https://doi.org/10.1016/j.jastp.2015.05.007

Huang, S. Y., Zhou, M., Deng, X. H., Yuan, Z. G., Pang, Y., Wei, Q., et al. (2012). Kinetic structure and wave properties associated with sharp dipolarization front observed by Cluster. *Annales de Geophysique*, *30*, 97–107. https://doi.org/10.5194/angeo-30-97-2012

McFadden, J. P., Carlson, C. W., Larson, D., Ludlam, M., Abiad, R., Elliott, B., et al. (2008). The THEMIS ESA Plasma Instrument and in-flight calibration. *Space Science Reviews*, *141*, 277–302. https://doi.org/10.1007/s11214-008-9440-2

Nakamura, R., Baumjohann, W., Klecker, B., Bogdanova, Y., Balogh, A., Rème, H., et al. (2002). Motion of the dipolarization front during a flow burst event observed by Cluster. *Geophysical Research Letters*, *29*(20), 1942. https://doi.org/10.1029/2002GL015763

Nakamura, R., Baumjohann, W., Schödel, R., Brittnacher, M., Sergeev, V. A., Kubyshkina, M., et al. (2001). Earthward flow bursts, auroral streamers, and small expansions. *Journal of Geophysical Research*, *106*, 10,791–10,802. https://doi.org/10.1029/2000JA000306

Nishimura, Y., Yang, J., Pritchett, P. L., Coroniti, F. V., Donovan, E. F., Lyons, L. R., et al. (2016). Statistical properties of substorm auroral onset beads/rays. *Journal of Geophysical Research: Space Physics*, *121*, 8661–8676. https://doi.org/10.1002/2016JA022801

Panov, E. V., Nakamura, R., Baumjohann, W., Kubyshkina, M., Artemyev, A., Sergeev, V. A., et al. (2012). Kinetic ballooning/interchange instability in a bent plasma sheet. *Journal of Geophysical Research*, *117*, A06228. https://doi.org/10.1029/2011JA017496

Panov, E. V., & Pritchett, P. L (2018). Dawnward drifting interchange heads in the Earth's magnetotail. *Geophysical Research Letters*, *45*, 8834–8843. https://doi.org/10.1029/2018GL078482

Panov, E. V., Sergeev, V. A., Pritchett, P. L., Coroniti, F. V., Nakamura, R., Baumjohann, W., et al. (2012). Observations of kinetic ballooning/interchange instability signatures in the magnetotail. *Geophysical Research Letters*, *39*, L08110. https://doi.org/10.1029/2012GL051668

Perraut, S., Le Contel, O., Roux, A., & Pedersen, A. (2000). Current-driven electromagnetic ion cyclotron instability at substorm onset. *Journal of Geophysical Research*, *105*, 21. https://doi.org/10.1029/2000JA900059

Pritchett, P. L., & Coroniti, F. V. (1994). Convection and the formation of thin current sheets in the near-Earth plasma sheet. *Geophysical Research Letters*, *21*, 1587–1590. https://doi.org/10.1029/94GL01364

Pritchett, P. L., & Coroniti, F. V. (1995). Formation of thin current sheets during plasma sheet convection. *Journal of Geophysical Research*, *100*, 23,551–23,566. https://doi.org/10.1029/95JA02540

Pritchett, P. L., & Coroniti, F. V. (1998). Interchange instabilities and localized high-speed flows in the convectively-driven near-Earth plasma sheet. In S. Kokubun & Y. Kamide (Eds.), *Substorms-4* (pp. 443–448). Dordrecht: Kluwer Academic Publishers.

Pritchett, P. L., & Coroniti, F. V. (2010). A kinetic ballooning/interchange instability in the magnetotail. *Journal of Geophysical Research*, *115*, A06301. https://doi.org/10.1029/2009JA014752

Pritchett, P. L., & Coroniti, F. V. (2011). Plasma sheet disruption by interchange-generated flow intrusions. *Geophysical Research Letters*, *38*, L10102. https://doi.org/10.1029/2011GL047527

Pritchett, P. L., & Coroniti, F. V. (2013). Structure and consequences of the kinetic ballooning/interchange instability in the magnetotail. *Journal of Geophysical Research: Space Physics*, *118*, 146–159. https://doi.org/10.1029/2012JA018143

Pritchett, P. L., Coroniti, F. V., & Nishimura, Y. (2014). The kinetic ballooning/interchange instability as a source of dipolarization fronts and auroral streamers. *Journal of Geophysical Research: Space Physics*, *119*, 4723–4739. https://doi.org/10.1002/2014JA019890

Pritchett, P. L., Coroniti, F. V., Pellat, R., & Karimabadi, H. (1991). Collisionless reconnection in two-dimensional magnetotail equilibria. *Journal of Geophysical Research*, *96*, 11. https://doi.org/10.1029/91JA01094

Rosenbluth, M. N., & Longmire, C. L. (1957). Stability of plasmas confined by magnetic fields. *Annals of Physics*, *1*, 120–140. https://doi.org/10.1016/0003-4916(57)90055-6

Roux, A., Perraut, S., Robert, P., Morane, A., Pedersen, A., Korth, A., et al. (1991). Plasma sheet instability related to the westward traveling surge. *Journal of Geophysical Research*, *96*, 17. https://doi.org/10.1029/91JA01106

Schindler, K., & Birn, J. (2004). MHD stability of magnetotail equilibria including a background pressure. *Journal of Geophysical Research*, *109*, A10208. https://doi.org/10.1029/2004JA010537

Sergeev, V. A., Gordeev, E. I., Merkin, V. G., & Sitnov, M. I. (2018). Does a local B-minimum appear in the tail current sheet during a substorm growth phase? *Geophysical Research Letters 45*, 2566–2573 https://doi.org/10.1002/2018GL077183

Sitnov, M. I., Merkin, V. G., Swisdak, M., Motoba, T., Buzulukova, N., Moore, T. E., et al. (2014). Magnetic reconnection, buoyancy, and flapping motions in magnetotail explosions. *Journal of Geophysical Research: Space Physics*, *119*, 7151–7168. https://doi.org/10.1002/2014JA020205
Sonnerup, B. U. Ö., & Scheible, M. (1998). Minimum and maximum variance analysis. *ISSI Scientific Reports Series*, *1*, 185–220.
Zhang, X., Angelopoulos, V., Pritchett, P. L., & Liu, J. (2017). Off-equatorial current-driven instabilities ahead of approaching dipolarization fronts. *Journal of Geophysical Research: Space Physics*, *122*, 5247–5260. https://doi.org/10.1002/2016JA023421
Zhou, M., Ni, B., Huang, S., Deng, X., Ashour-Abdalla, M., Nishimura, Y., et al. (2014). Observation of large-amplitude magnetosonic waves at dipolarization fronts. *Journal of Geophysical Research: Space Physics*, *119*, 4335–4347. https://doi.org/10.1002/2014JA019796